Supporting Information

Sefati et al. 10.1073/pnas.1309300110

SI Materials and Methods

Experimental Apparatus. The experimental test section of the flow tunnel (Fig. 2*A*) is ∼90 cm long, 25 cm wide, and 30 cm deep. Steady-state flow speed through the tunnel can be adjusted using a frequency controller connected to the electric pump. Flow speed in the test section was calibrated, as a function of pump frequency, by timing small drops of colored dye as they traversed a known distance through the test section at pump frequencies from 0 to 60 Hz in increments of 3 Hz, which resulted in flow speeds from 0 to 15 cm/s (flow speed = 0.25 × pump frequency, $R^2 = 0.996$).

A pco.1200s high-speed camera (Cooke Corp.) with a Micro-Nikkor 60-mm f/2.8D lens (Nikon, Inc.Y) captured video from below. The video was captured at 100 frames per second for all trials.

Ribbon Fin Tapers at Both Ends. The height of the ribbon fin is not constant along the body, and the fin is tapered at both ends. For use in a computational fluid model and calculation of amplitude of angular deflection of fin rays from the 2D motion of the ribbon fin (fin motion was captured from the bottom view as explained in *Materials and Methods*), the fin height profile, $h(x)$, was digitized for each individual fish. Fish were briefly anesthetized and positioned to capture a lateral image. The fin height profile of a representative trial is shown in Fig. S2. The blue curve depicts $h(x)$ and $-h(x)$ of an individual during steady-state swimming at $U = 3$ cm/s.

Amplitude of Angular Deflection. In a 2D snapshot of the ribbon fin captured from the bottom view, digitized peaks and troughs correspond to the fin rays that are oscillating with the amplitude of angular deflection at that instant (orange and green circles in Fig. 2*B*). Using all digitized peaks and troughs in 100 video frames, an envelope curve was calculated for each wave. In Fig. S2, envelopes for tail and head waves of a representative fish are shown in orange and green, respectively. At each tested flow speed, the amplitude of angular deflections for all fin rays along the tail and head waves, namely, θ_t and θ_h, were calculated by minimizing a sum of squared differences between the 2D projection of fin rays and the envelopes of digitized data from fin motion.

Computational Simulation. Here, we describe a computational model for computing the net force produced by a single traveling wave. During the derivation below, we suppress the subscripts t and h, which indicate tail and head waves, respectively, until we compute the overall forces F_t and F_h in Eq. **S10**, below.

As discussed in the main text, drag force applied to the propulsive infinitesimal element is given by:

$$d\vec{\mathbf{F}} = \frac{1}{2} C_D \rho dA \left[\vec{\mathbf{u}} \cdot \vec{\mathbf{n}}_s\right]^2 \vec{\mathbf{n}}_s, \qquad \text{[S1]}$$

where C_D is the coefficient of the drag, ρ is the density of the fluid, dA is the area of the infinitesimal element, and $\vec{\mathbf{n}}_s$ is the unit normal to the surface at the centroid of the infinitesimal element (see below). The function $\vec{\mathbf{u}}(x,r)$ is the relative velocity of the centroid of the element on the fin and steady-state flow speed:

$$\vec{\mathbf{u}}(x,r) = u_{\text{fin}}(x,r) \pm U\vec{\mathbf{i}}. \qquad \text{[S2]}$$

The sign of the last term is negative for the rostral wave and positive for the caudal wave, and

$$u_{\text{fin}}(x,r) = r\frac{\partial\theta}{\partial t}\left(\sin\theta\,\vec{\mathbf{j}} + \cos\theta\,\vec{\mathbf{k}}\right), \qquad \text{[S3]}$$

where r is the radial distance from the base of the fin ray to the centroid of the infinitesimal element, x is the rostrocaudal coordinate of the element, and θ is angle of the fin for the two waves, as defined in Eq. **4**.

The 2D surface of a rectangular ribbon fin can be parameterized as a set of points in three dimensions:

$$\vec{\mathbf{H}} = x\vec{\mathbf{i}} - r\cos\theta\,\vec{\mathbf{j}} + r\sin\theta\,\vec{\mathbf{k}}. \qquad \text{[S4]}$$

Here, $x \in [L_{\min}, L_{\max}]$ is defined over the half-wave of interest, and the range of $r \in [0, h(x)]$ depends on the fin profile function, $h(x)$ (see above).

Geometric properties of the surface, such as the unit normal vector, $\vec{\mathbf{n}}_s$, of the surface at each point, can be derived from the metric tensor (1):

$$\vec{\mathbf{n}}_s = \frac{1}{\sqrt{1+r^2\theta_x^2}}\left[-r\theta_x\vec{\mathbf{i}} + \sin\theta\,\vec{\mathbf{j}} + \cos\theta\vec{\mathbf{k}}\right], \qquad \text{[S5]}$$

where θ_x is $\frac{\partial\theta}{\partial x}$.

Note that the normal, $\vec{\mathbf{n}}_s$, is defined relative to one side of the fin but that at each local peak or trough of the fin, there is a switch in which side of the fin is traveling "upstream"; this switch depends on both the sign of θ_x and the wave direction, which is different for the head and tail waves. Thus, the normal vector for each infinitesimal element on the surface of the fin is $\vec{\mathbf{n}} = \pm\vec{\mathbf{n}}_s$. Using the normal vector for each differential element, we have

$$\vec{\mathbf{u}} \cdot \vec{\mathbf{n}} = \frac{(\lambda f \pm U)}{\sqrt{1+r^2\theta_x^2}}(r|\theta_x|) \qquad \text{[S6]}$$

$$= \frac{(V \pm U)}{\sqrt{1+r^2\theta_x^2}}(r|\theta_x|), \qquad \text{[S7]}$$

where $V - U$ corresponds to the head wave and $V + U$ corresponds to the tail wave. Instantaneous net force is computed by integrating $d\vec{\mathbf{F}}$ over the half-wave of interest; the two half-wave forces can then be added to compute the total force on the fin. The time-averaged force over one period of fin undulation is zero for y and z (lateral) components; this can be seen by the periodic y and z components in the unit normal vector shown in Eq. **S5**. The time-averaged thrust force generated by each half-wave in the x direction can be computed by

$$|F_x| = \frac{1}{T}\int_0^T\int_{L_{\min}}^{L_{\max}}\int_0^{h(x)}\left(d\vec{\mathbf{F}}\cdot\vec{\mathbf{n}}_x\right)dr\,dx\,dt$$

$$= \frac{1}{T}\frac{\rho C_D}{2}\left(\frac{2\pi\theta_m}{\lambda}\right)^3(V \pm U)^2$$

$$\int_0^T\int_{L_{\min}}^{L_{\max}}\int_0^{h(x)}\frac{r^3\left|\cos 2\pi\left(\frac{x}{\lambda} \mp ft\right)\right|^3}{\left(1+r^2\theta_x^2\right)^{3/2}}dr\,dx\,dt, \qquad \text{[S8]}$$

where $\vec{\mathbf{n}}_x$ is the unit vector in the x direction, $V - U$ corresponds to the head wave, and $V + U$ corresponds to the tail wave. In the

analysis of forces generated by the fin, we use the kinematic parameters measured for each individual trial (frequency, wavelength, and amplitude of angular deflection), which are assumed to remain constant over one period of undulation. The fin height function for each fish, $h(x)$, is obtained via digitization of the fin profile (see above for experimental methods). The net thrust force, generated by the ribbon fin, is the summation of thrust forces generated by two half-waves.

Plant Model for Station Keeping in *Eigenmannia*. In addition to the detailed force analysis for each biological trial, in which the digitized height profile is taken into account, we further approximate the fin to capture the essential structure of counterpropagating wave mechanics in a lumped-parameter model. We assume the fin has a rectangular profile [i.e., the height of fin is the same along the length of fin (note that this matches the morphology of our biomimetic robot)]. Because we are averaging the force over one period of oscillation ($T = 1/f$), for a fixed r in Eq. **S8**, the integrand becomes independent of variable x. Thus, the time-averaged generated thrust is $F \propto L_{\text{fin}}(V \pm U)^2$, where L_{fin} is the length of the fin, V is the wave speed along the fin, and U is the steady-state flow speed. Net force over the body includes the thrusts generated by the two waves and drag force over the body:

$$F_{\text{net}} = F_t + F_h + F_{\text{drag}}, \qquad \textbf{[S9]}$$

where subscripts t and h stand for tail and head, respectively. If we take $L_{\text{head}} = L_{\text{tail}} = L/2$ as the reference for the nodal shift, $\Delta L = 0$, the generated thrust by each wave is:

$$\begin{aligned} F_t &= -a(L/2 - \Delta L)(V + U)^2\,\vec{\mathbf{i}} \\ F_h &= a(L/2 + \Delta L)(V - U)^2\,\vec{\mathbf{i}}, \end{aligned} \qquad \textbf{[S10]}$$

where a is a constant. The simplified expression for the net thrust generated by the two waves is:

$$F_t + F_h = \left(\kappa + \gamma U^2\right)\Delta L - \beta U, \qquad \textbf{[S11]}$$

where $\kappa = 2aV^2$, $\gamma = 2a$, and $\beta = 2aLV$. For low-speed swimming ($U^2 \approx 0$), the last equation can be further simplified to:

$$F_t + F_h = \kappa \Delta L - \beta U. \qquad \textbf{[S12]}$$

For low-speed swimming, the drag force over the body is also negligible ($F_{\text{drag}} \approx 0$). Moreover, during steady-state swimming, the net force over the body has to sum to zero, $F_{\text{net}} = 0$. Thus, antagonistic forces generated by two waves should balance each other according to Eq. **S9** ($F_t + F_h \approx 0$). The second-order lumped model can be used as a task-level plant model of the ribbon fin for low-speed refuge tracking:

$$m\ddot{x} + \beta\dot{x} = u(t), \qquad \textbf{[S13]}$$

where β is the damping constant and $u(t)$ is the net thrust generated by the ribbon fin. In the case of counterpropagating waves, $u(t) = \kappa \Delta L$, where κ is the nodal shift gain.

Linear Quadratic Controller to Track a Reference Trajectory. The second-order lumped model (Eq. **S13**) can be written in state space:

$$\dot{\mathbf{x}} = A\mathbf{x} + Bu(t), \qquad \textbf{[S14]}$$

where $A = [0\ 1;\ 0\ -\ b/m]$ and $B = [0;\ 1/m]$, with the state vector containing the position and velocity $\mathbf{x} = [x; \dot{x}]$. By discretizing the linear system, an optimal affine control law exists according to table 4.4-1 in ref. 2.

Mechanical Energy During Tracking and Hovering. In the limit, as the tracking amplitude goes to zero (and assuming no disturbances), the mechanical work done by a single traveling wave is zero, but even for perfect hovering, counterpropagating waves are continuously doing work on the surrounding fluid. It is natural to ask whether it remains costly to use counterpropagating waves during tracking behavior.

To examine this question, we estimated the worst case mechanical energy required for a single traveling wave for the largest amplitude tracking motion compared with the energy required for simple hovering using counterpropagating waves as a conservative measure of how much more it costs the animal to use this strategy.

The instantaneous power from each infinitesimal element is given by $dP = -d\vec{\mathbf{F}} \cdot \vec{\mathbf{u}}$, where $\vec{\mathbf{u}}$ is the instantaneous velocity of the element relative to the fluid and $-d\vec{\mathbf{F}}$ is the force applied by each infinitesimal element of the fin to the fluid. Total power was estimated by integrating the dP over the fin. Mechanical work over each cycle was then estimated by integrating $P(t)$ over one period (5 s) of the tracking task (Fig. 5).

SI Data and Discussion

Other Wave Parameters Varied Minimally with Flow Speed. For each trial, wavelengths of the tail and head waves, λ_t and λ_h, were computed by averaging the rostrocaudal distances between all adjacent pairs of peaks and troughs in each wave over 100 video frames (Fig. S3*A*). The tail and head wavelengths varied minimally as a function of flow speed, trending downward and upward slightly for tail and head waves, respectively, at the highest swimming speeds. Similarly, the maximum angular deflection of both waves varied minimally as a function of steady-state flow speed (Fig. S3*B*). The temporal frequency of tail and head waves (f_T and f_H) was calculated for all trials. For the four trials at $U =$ 12 cm/s, there was only one single traveling wave from head to tail. Temporal frequencies averaged over all trials as a function of steady-state swimming speeds are shown in Fig. S3*C*. Using the data shown in Fig. S3 *A* and *C*, wave speeds ($V = \lambda f$) of the tail and head waves are shown in Fig. S3*D*. At lower swimming speeds, where we believe the counterpropagating waves strategy is the dominant mechanism for control, the wave speeds of the two waves (product of wavelength and temporal frequency) are very similar. Note that despite differences in frequency and wavelength, these differences result in roughly equal wave speed in the two waves; that is, the two waves travel at approximately the same speed during slow swimming (i.e., near hovering). The difference becomes more significant at higher swimming speeds. Although beyond our present scope, this deviation could possibly be explained by the transition from the counterpropagating waves strategy to the single traveling wave strategy. In other words, although nodal shift serves as the dominant strategy for modulating the thrust force at low-speed swimming, the role of other kinematics, such as frequency and wavelength, may become important at higher swimming speeds. Lastly, the tail wave becomes very short (shorter than one complete wavelength) at the highest swimming speeds tested. As a result, there may be subtle artifacts associated with estimating the tail wavelength in the digitization process.

In Fig. S3, the shaded regions depict the entire range of variation across all trials and all individuals. Although there was moderate variability across individuals, each individual was extremely consistent. At each tested flow speed, the SD of the angular deflection for each of the five individual fish was between 0.1° and 7.2° for the tail wave (θ_t) and between 0.1° and 4.7° for the head wave (θ_h). Similarly, the SD of the wavelength for each of the five individual fish was between 0.1 cm and 0.26 cm for the tail wave (λ_t) and between 0.1 cm and 0.3 cm for the head wave (λ_h). The SD of frequency for each of five individual fish was between 0.1 Hz and 2.3 Hz for the tail wave (f_t) and between

0.1 Hz and 1.6 Hz for the head wave (f_t). The SD of wave speed for each of five individual fish was between 0.02 cm/s and 4.85 cm/s for the tail wave (V_t) and between 0.01 cm/s and 1.84 cm/s for the head wave (V_h).

Counterpropagating Waves Modulate Fore–Aft Thrust for Hovering. During station keeping, the net forces over the body include the antagonistic thrust forces generated by the head and tail waves, as well as the drag force over the body and pectoral fins. Although nonzero net force is necessary for transient movement and unsteady swimming, net forces over the fish body must sum to zero during station keeping.

Eigenmannia modulates net thrust, generated by the two waves, mainly by moving the nodal point. When there is no ambient flow, the nodal point remains near the middle of the fin. If the ribbon fin were not tapered at its ends and the kinematic parameters of the two counterpropagating waves were identical, then, in theory, the nodal point would be exactly in the middle of the fin. For relatively slow flow speeds (i.e., under 12 cm/s in this study), the tail wave travels against the flow, whereas the head wave travels along with, although faster than, the flow. Moreover, the nodal point moves caudally as the steady-state swimming speed increases during upstream station keeping. This produces two competing effects in the amount of force generated by each wave: a change of length (and thus area) of each wave and a change in the relative velocity between the waves and the ambient flow. Although the tail wave (L_{tail}) shortens, the relative velocity between the tail wave speed ($V_t = \lambda_t f_t$) and flow speed (U) increases [$V_t - (-U) = U + V_t$]. By contrast, although the head wave (L_{head}) lengthens, the relative velocity between the head wave speed ($V_h = \lambda_h f_h$) and flow speed [$-V_h - (-U) = U - V_h$] decreases. As a result of these two competing effects (i.e., decrease/increase in fin length and increase/decrease in relative velocity between the ribbon fin wave speeds and the flow speed), antagonistic forces generated by the two waves balance each other during station keeping.

Outlier Replicate in Biological Data. As explained in the main text, the kinematics of the ribbon fin of five fish were digitized in this study, and at each tested flow speed, three replicates of data were collected. The nodal shift of the third replicate collected for fish 3 followed the qualitative trends of other replicates but was an outlier quantitatively. Measured nodal shift of this replicate is shown with a different color (purple) in Fig. S4.

Nodal Shift Gain in Robot and *Eigenmannia*. Kinematic parameters used for the robotic experiment are shown in Table S1. In each trial, the net longitudinal force was measured as a function of nodal shift. Nodal position was varied from −8.15 cm to 8.15 cm, measured from the middle point along the fin, with 1.63-cm increments. The increment of 1.63 cm was equivalent to 5% of the robotic fin length. In Fig. S5 *A* and *B*, the measured forces are shown as a function of nodal shift. Results reveal that the thrust varies linearly as a function of nodal shift. Fig. S5 *A* and *B* also reveals that the nodal shift gain increases as the temporal frequencies of counterpropagating waves and the amplitude of angular deflection of fin rays increase, respectively. Nodal shift gains, corresponding to the results shown in Fig. S5*A*, as a function of temporal frequency (f) are depicted in Fig. S5*C*. Nodal shift gain, κ, is increasing roughly quadratically as a function of frequency, f.

Finally, using the kinematics measured corresponding to hovering in biological experiments, nodal shift gain was estimated for *Eigenmannia*. In each set of simulations, the kinematic and morphological parameters of the model were set to match the kinematics measured with no ambient flow trial ($U = 0$) in the biological experiments. Nodal position was varied from −10 mm to 10 mm. Simulation results for three replicates of a representative fish are depicted in Fig. S5*D*. Forces generated by the head wave, tail wave, and net thrust are shown for three replicates. Each color represents the result for one replicate (set) of data. The results reveal that the force generated by the two waves increases linearly as a function of nodal position. Simulation results for four other individual fish are similar to the results shown in Fig. S5*D*. The nodal shift gain, κ, was 0.0209 N/m (SD = 0.0084 N/m) over all replicates of data.

Damping Constant in Robot and *Eigenmannia*. Kinematic parameters used for the robotic experiment and simulation were the same as those shown in Table S2. The nodal point was held at the center of the robotic fin ($\Delta L = 0$); thus, the lengths of the two counterpropagating waves were equal. Ambient flow speed was varied from 0 cm/s to 10 cm/s with 0.5-cm/s increments. Only the robotic fin was submerged in this experiment. The measured forces as a function of steady-state ambient flow are shown in Fig. S6 A and *B*. From Fig. S6 *A* and *B*, it can also be observed that the damping constant increases as the temporal frequencies of counterpropagating waves and the amplitude of angular deflection of fin rays increase. Damping constants, corresponding to the results shown in Fig. S6*A*, as a function of temporal frequency (f) are depicted in Fig. S6*C*. The damping constant, β, is increasing linearly as a function of temporal frequency, f.

Finally, the damping constant was calculated for the *Eigenmannia*. Similar to the simulations explained in the previous section, in each set of simulations, kinematic parameters of the model were set to the kinematics captured during zero flow speed ($U = 0$) in the biological experiment. The nodal position remained fixed at $\Delta L = 0$. The steady-state flow speed was varied from −5 cm/s to 5 cm/s. Predicted forces generated by each wave and the net force are shown in Fig. S6*D*, and, as shown, the damping forces increase linearly as a function of nodal position. Simulation results for four other individual fish are similar to the results shown in Fig. S6*D*. The damping constant, β, was 0.0053 N·s·m (SD = 0.0019 N·s·m) over all replicates.

Mechanical Energy Cost of Counterpropagating Waves. We estimated the mechanical cost of counterpropagating waves during hovering and compared this with the cost during high-amplitude tracking using a single traveling wave (*SI Materials and Methods*).

For the fish, hovering with counterpropagating waves requires 1.1 mJ of mechanical work in 5 s, whereas high-amplitude tracking using a single traveling wave requires 0.35 mJ. Likewise, for the robot, hovering with counterpropagating waves requires 1.7 J of mechanical work in 5 s, whereas high-amplitude tracking using a single traveling wave requires 0.4 J. That is, for our setting, the mechanical energetic cost of counterpropagating waves is at least threefold that of single traveling waves.

The mechanical energy required by each strategy is a factor that contributes to metabolic cost, but we cannot conclude that the differences in metabolic cost are commensurate to those in mechanical energy. Moreover, it is unknown whether the metabolic expenditure for either strategy is significant with respect to the metabolic budget.

1. Chirikjian GS (2009) Stochastic models, information theory, and lie groups. *Classical Results and Geometric Methods (Applied and Numerical Harmonic Analysis)* (Birkhäuser, Boston), Vol 1.

2. Lewis FL, Syrmos VL (1995) *Optimal Control* (Wiley, New York).

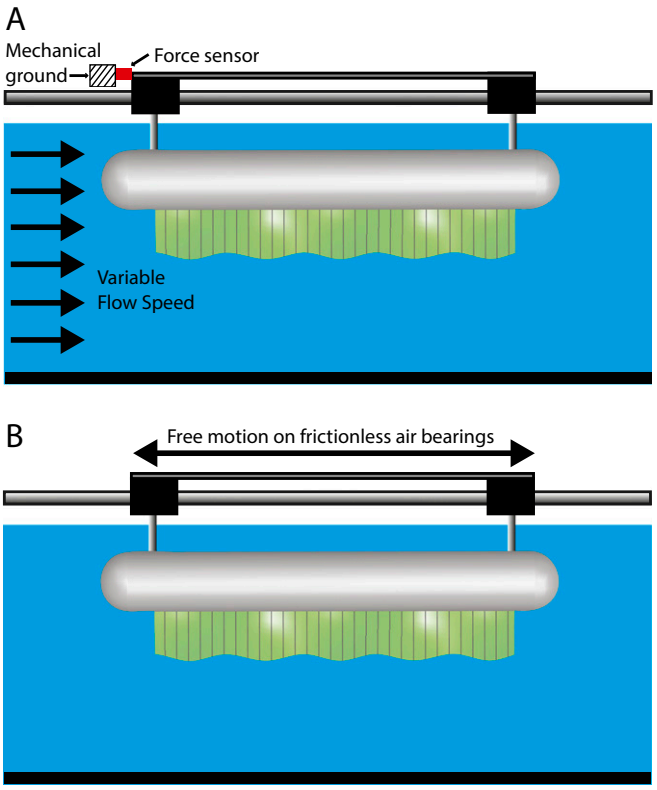

Fig. S1. Experimental setup for the knifefish robot. (*A*) Knifefish robot was suspended into a water tunnel from a frictionless air-bearing system above. To measure force, the platform was rigidly attached to mechanical ground through a force sensor. Force measurements were collected for varying fin kinematics and flow speeds. (*B*) For the virtual refuge tracking experiments, the robot was allowed to move freely along the longitudinal axis. A linear encoder provided positional feedback of the robot. Experiments included controlling either fin oscillation frequency or nodal shift of counterpropagating waves to follow sinusoidal trajectories of varying frequency and amplitude.

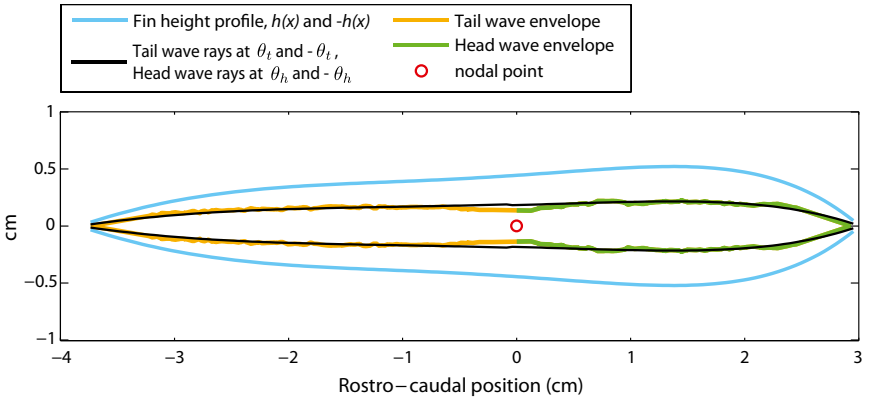

Fig. S2. In the 2D bottom view, the ribbon fin is tapered at both ends. The fin height profile was digitized for each individual fish. The fin height profile for a representative fish is shown in blue. The envelope of all digitized peaks and troughs is shown in orange (tail wave) and green (head wave). 2D visualization of the fin with fitted θ_t and θ_h is shown in black.

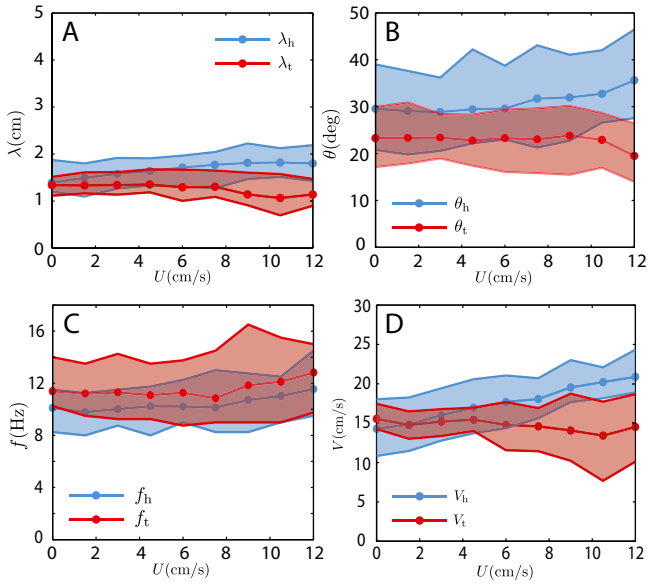

Fig. S3. Ribbon fin kinematics as a function of steady-state flow speed. At each tested flow speed, the averages over all replicates of data are shown with a filled circle. Shaded regions indicate the full range of a given kinematic parameter for all trials and all fish. (*A*) Wavelength of the tail (red) and head waves (blue) remain nearly constant across flow speeds. (*B*) Angular amplitudes of the tail wave (red) and head wave (blue) also remain nearly consistent across flow speeds, although there is a small trend, particularly for the tail wave. (*C*) Similar to wavelength and angular amplitude, the temporal frequency of the tail wave and head wave also remains nearly constant, particularly for lower swimming speeds. (*D*) Wave speeds $(V = \lambda f)$ of the tail (red) and head (blue) waves are roughly equal at lower swimming speeds.

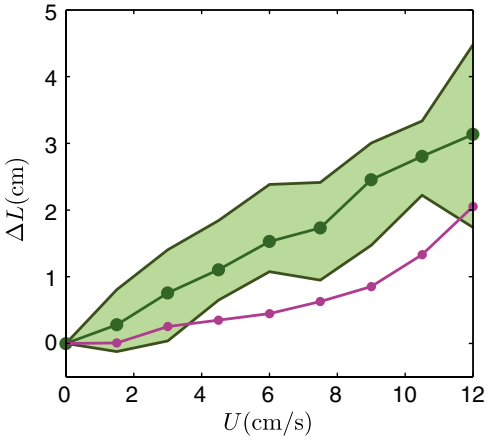

Fig. S4. One replicate of data was removed from the statistics. The measured nodal shift for the outlier replicate is shown in purple.

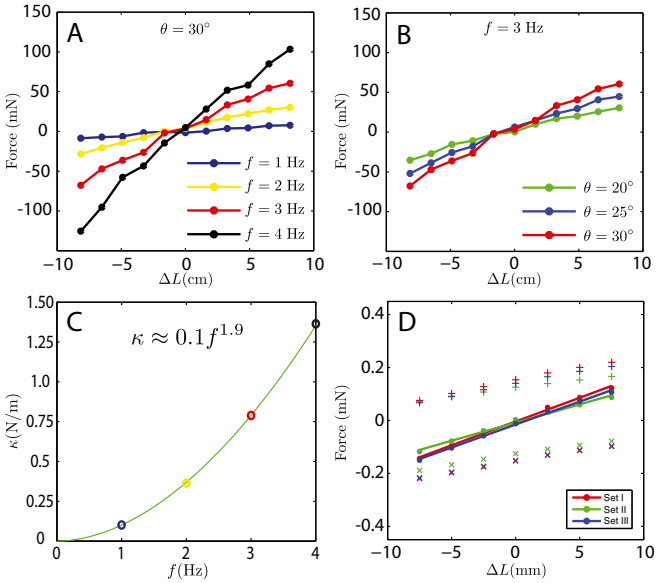

Fig. S5. Force measurements from the robotic setup (nodal point shift gain). (*A*) For a constant angular amplitude ($\theta = 30°$), forces generated by robotic fin are shown for different frequencies. (*B*) For a constant frequency ($f = 3$ Hz), forces generated by robotic fin are shown for different angular amplitudes. (*C*) Nodal shift gains computed from a linear fit to the results shown in *A* are depicted as a function of frequency. κ varies nonlinearly as a function of *f*. (*D*) Computational results. Measured kinematics of fish 4 from three replicates of the data during hovering (no ambient flow) are used as inputs for the computational model. Computed forces as a function of nodal shift (ΔL) are shown. The three colors (red, green, and blue) correspond to three replicates (sets) of data. Forces generated by the head wave (+), forces generated by the tail wave (x), and the net force produced by the two waves (filled circles) are shown.

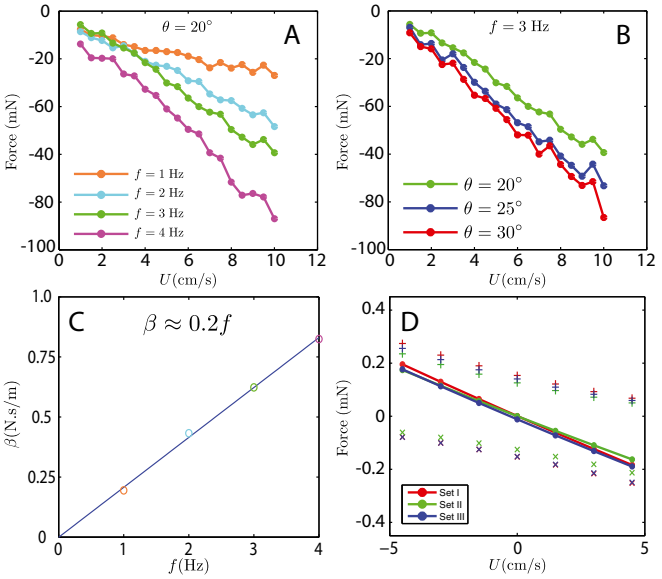

Fig. S6. Force measurements from the robotic setup (damping constant). (*A*) For a constant angular amplitude ($\theta = 20°$), forces acting on the robotic fin are shown for different frequencies. (*B*) For a constant frequency ($f = 3$ Hz), forces acting on the robotic fin are shown for different angular amplitudes. (*C*) Damping constants computed from a linear fit to the results shown in *A* are depicted as a function of frequency. β varies linearly as a function of *f*. (*D*) Computational results. Measured kinematics of fish 4 from three replicates of the data during hovering (no ambient flow) are used as inputs for the computational model. Computed forces over the ribbon fin are shown as a function of steady-state flow speed (*U*). The three colors (red, green and blue) correspond to three replicates (sets) of data. Forces generated by the head wave (+), forces generated by the tail wave (x), and the net force produced by the two waves (filled circles) are shown.

Table S1. Fin kinematic parameters for force measurement in the first robotic experiment

Experimental set	f, Hz	θ,°	No. of waves, L_{fin}/λ
Set 1	1, 2, 3, 4	30	4
Set 2	3	20, 25, 30	4

Table S2. Fin kinematic parameters for force measurement in the second robotic experiment

Experimental set	f, Hz	θ,°	No. of waves, L_{fin}/λ
Set 1	1, 2, 3, 4	20	4
Set 2	3	20, 25, 30	4

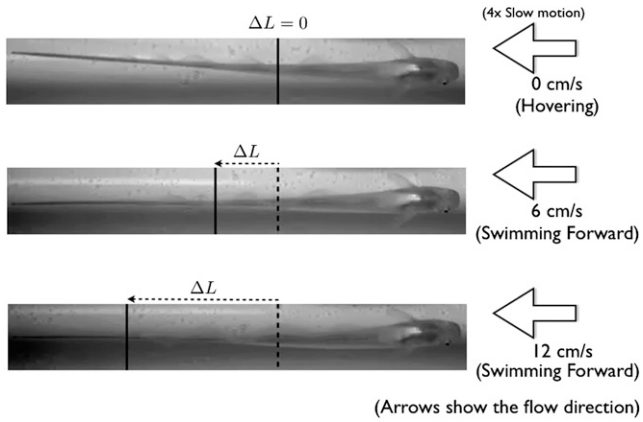

Movie S1. Counterpropagating waves at three different steady-state swimming speeds (U = 0, 6, and 12 cm/s) captured using high-speed videography.

Movie S1

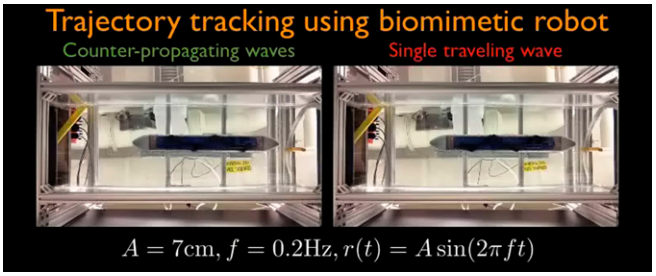

Movie S2. Biomimetic robot tracking with two control strategies.

Movie S2

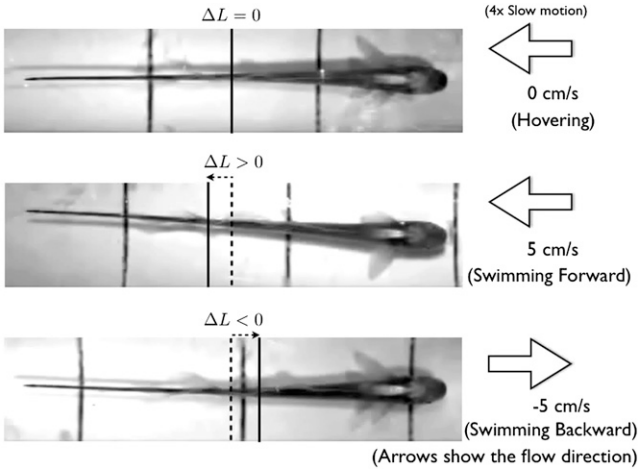

Movie S3. Counterpropagating waves during hovering and swimming forward and backward captured using high-speed videography.

Movie S3